Development of a Self-Consistent Poisson-Schrödinger Solver

Geoffrey Xiao

I. Introduction

The Poisson-Schrödinger (PS) model is widely used to simulate devices in which quantum confinement of charge carriers plays a major role[1-4]. Advances in materials growth, through techniques such as molecular beam epitaxy (MBE) and pulsed laser deposition (PLD), have allowed for the growth of material heterostructures where sharp band offsets can confine carriers in quantum wells. In these structures, quantum mechanical treatments must supplant classical ones. By using the effective mass approximation and the band structure as the confining potential for mobile charge carriers (holes ad electrons), the charge density can be determined using Schrödinger's equation. Using the charge density, the Poisson equation can give the band structure. The coupling of the two equations requires a self-consistent approach.

Currently, many Poisson-Schrödinger solvers exist. From Dr. Gregory Snider's 1D PS Solver[5] to nextnano[6], a company devoted to providing 1D, 2D, and 3D PS simulations, there are a wealth of commercial and freeware PS utilities. Nevertheless, building the code from the fundamentals allows for a tremendous learning experience. Practically speaking, a home-built PS Solver allows for greater control over the simulation parameters; the code is not simply a "black box" system—it can be tailored to suit specific aims and needs.

Here, a 1D PS solver is developed using MATLAB. The development of the solver is presented step-by-step to definitively show that the parts of the solver work as intended. Parts II through V discuss, with examples, the constituent elements of the PS solver. In Parts VI and VII, two heterostructures will be simulated to show that the complete PS solver works. Ultimately, the goal is to use the solver to simulate the conduction and valence bands of complex oxide heterostructures grown by PLD. Knowledge of the band structures provides a valuable theoretical supplement to photoluminescence and other characterization experiments performed on these material heterostructures.

II. Schrödinger Equation

Crucial to solving the coupled Poisson-Schrödinger equation is solving the time-independent Schrödinger equation. The hallmark of quantum mechanics, the Schrödinger equation describes the behavior of a quantum mechanical particle with a wavefunction. Encapsulated in the wavefunction are all the observables, such as kinetic energy, momentum, and position, of the particle. Unfortunately, analytical solutions to the Schrödinger equation exist only for few a physical systems. To this end, three different numerical methods were developed to solve the equation. Because different numerical methods independently give similar solutions and because the numerical solutions agree with literature

and analytical results, there is high confidence that the Schrödinger equation part of the PS solver works.

Constant Mass Schrödinger Equation

If the particle's mass $m(x)$ is independent of position, the Schrödinger equation is:

$$\left[\frac{-\hbar^2}{2m^*}\frac{d^2}{dx^2} + V(x)\right]\psi(x) = \hat{H}\psi(x) = E\psi(x) \tag{1}$$

$$\frac{d^2}{dx^2}\psi(x) = \frac{2m^*}{-\hbar^2}[E - V(x)]\psi(x) \tag{2}$$

In Equations 1 and 2, $\hbar$ is the reduced Planck's constant, E is the eigenenergy, $V(x)$ is the potential function that characterizes the physical system, $\psi(x)$ is the wavefunction, m^* is the effective mass, and $\hat{H}$ is the Hamiltonian operator. Two methods can solve Equation 1: basis set expansion[7] and numerical integration[8]. In basis set expansion, the wavefunction is expressed as a linear combination of orthogonal functions. Through mathematical manipulations, the Schrödinger equation is converted into a matrix eigenvalue problem that can be easily solved on a computer. Appendix A describes the details of the basis set expansion method.

In numerical integration, various derivative approximations can replace the second derivative with a finite difference equation. Two numerical integration schemes were used: Numerov's method and the fourth order Runge-Kutta method (RK4). In each of these methods, the wavefunction can be integrated numerically, but only certain values of E will give wavefunctions that satisfy the boundary conditions. The goal, then, is to find the E that give wavefunctions satisfying the boundary conditions: these are the eigenenergies and corresponding eigenwaves for the system. Appendices B and C discuss the Numerov and Runge-Kutta methods respectively.

Finite Square Well

The finite square well is one of the few potentials for which an analytical solution exists. Table 1 below compares the analytical[9] and numerical simulation results for an electron in a finite square well of width 0.5 nm and depth 25 eV. The agreement between all four methods is very close leading to a high confidence in the code. The first two wavefunctions solved via basis set expansion are shown in Figure 1 The Numerov and RK4 wavefunctions are identical to the basis set expansion wavefunctions shown in Figure 1.

Table 1. Eigenvalues for the finite square well.

Eigenvalues (eV)				
Energy Level	Analytical[9]	Basis Set Expansion	Numerov	RK4
1	1.123	1.123	1.123	1.123
2	4.461	4.463	4.463	4.463
3	9.905	9.910	9.932	9.871
4	17.162	17.171	17.148	17.170
5	24.782	24.789	24.818	24.7819
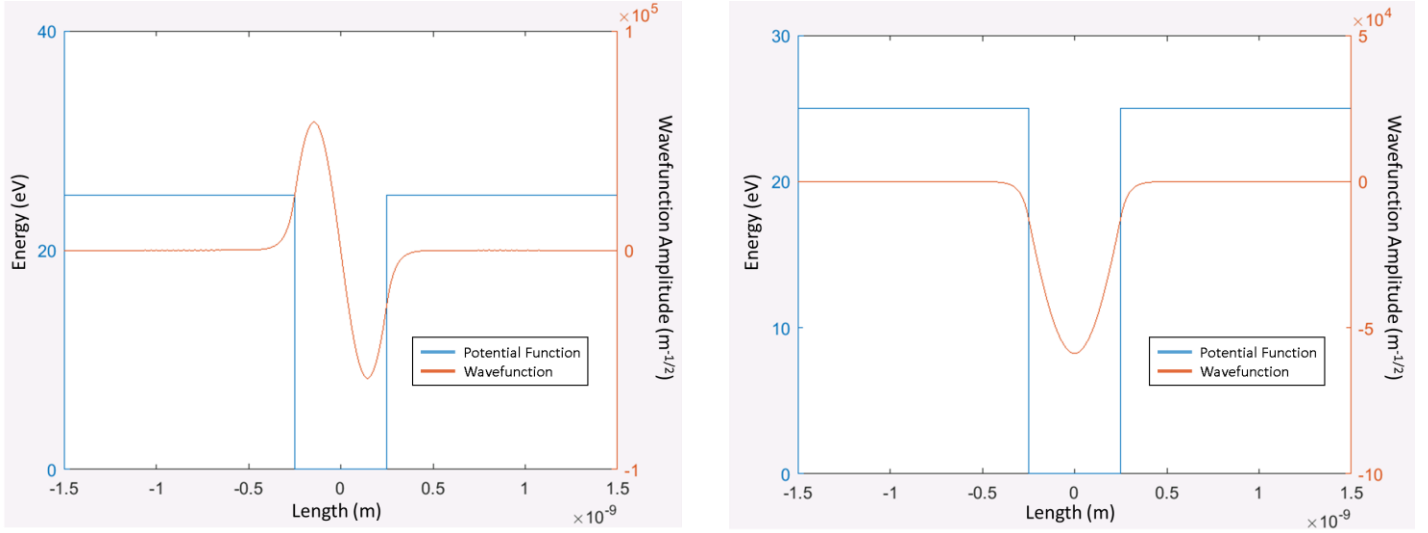
Figure 1. The first two wavefunctions as solved by basis set expansion.

Variable Mass Schrödinger Equation

Many of the interesting applications involve heterostructures, which are composed of several different materials. Therefore, the mass cannot simply be assumed to be position-independent. To this end, the variable mass Schrödinger equation must be solved. The Hamiltonian operator in Equation 1 is not Hermitian for a variable mass[10]. Several versions of the Hamiltonian operator have been developed for particles with variable mass. Here, the following version of the Schrödinger equation is used[10]:

$$\left[\frac{-\hbar^2}{2}\frac{d}{dx}\left(\frac{1}{m(x)}\frac{d}{dx}\right) + V(x)\right]\psi(x) = E\psi(x) \tag{3}$$

The Numerov method cannot integrate the variable mass Schrödinger equation. Nonetheless, the Runge-Kutta and basis set expansion methods can be used to solve Equation 3. Several cases are presented below to show that the developed code adequately solves for the eigenvalues of a variable mass quantum system.

Free Particle Potential with Soliton Mass Profile
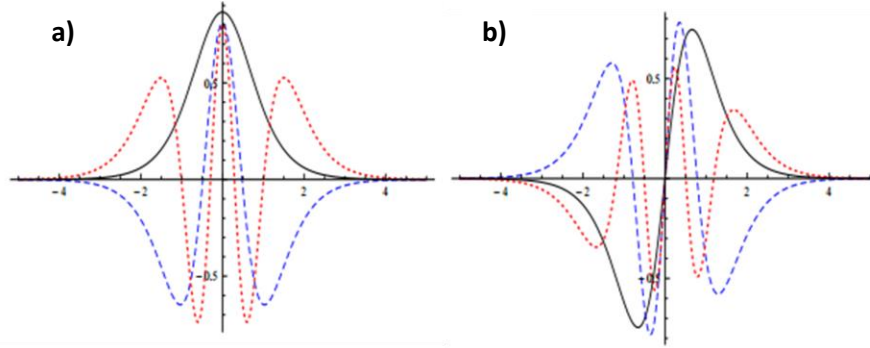
For the following conditions:

$$\text{Potential: } V(x) = 0 \tag{4}$$

$$\text{Mass profile: } m(x) = m_0 \operatorname{sech}^2(ax), \tag{5}$$

it was found that the eigenvalues are[11]:

$$E_n = \frac{a^2\hbar^2}{2m_0}n(n+1), n > 0. \tag{6}$$

The corresponding wavefunctions are shown in Figure 2. In Figure 2a, the black, blue, and red are the n = 1, 2, and 3 wavefunctions, respectively. In Figure 2b, the black, blue, and red are the n = 2, 4, 6 wavefunctions, respectively.


Figure 2. a) The black, blue, and red are the n = 1, 3, and 5 wavefunctions, respectively[11]. **b)** The black, blue, and red are the n = 2, 4, and 6 wavefunctions, respectively[11].

The eigenvalues determined using the basis set expansion and Runge-Kutta methods are tabulated in Table 2. The energies follow a $n * (n + 1)$ relationship, as specified by Equation 6.

Table 2. The eigenvalues for the soliton mass profile free particle potential.

Eigenvalue index, n	RK4 (eV)	$\frac{RK4}{n*(n+1)}$ (eV)	Basis Set Expansion (eV)	$\frac{Basis\ Set}{n*(n+1)}$ (eV)
1	0.000489	0.000245	0.000488	0.000244
2	0.001468	0.000245	0.001467	0.000245
3	0.002939	0.000245	0.002934	0.000245
4	0.004905	0.000245	0.00492	0.000246
5	0.007367	0.000246	0.007363	0.000245
6	0.010325	0.000246	0.010341	0.000246

The first four wavefunctions solved with the basis set expansion are shown in Figure 3. These agree nicely with those in Figure 2.
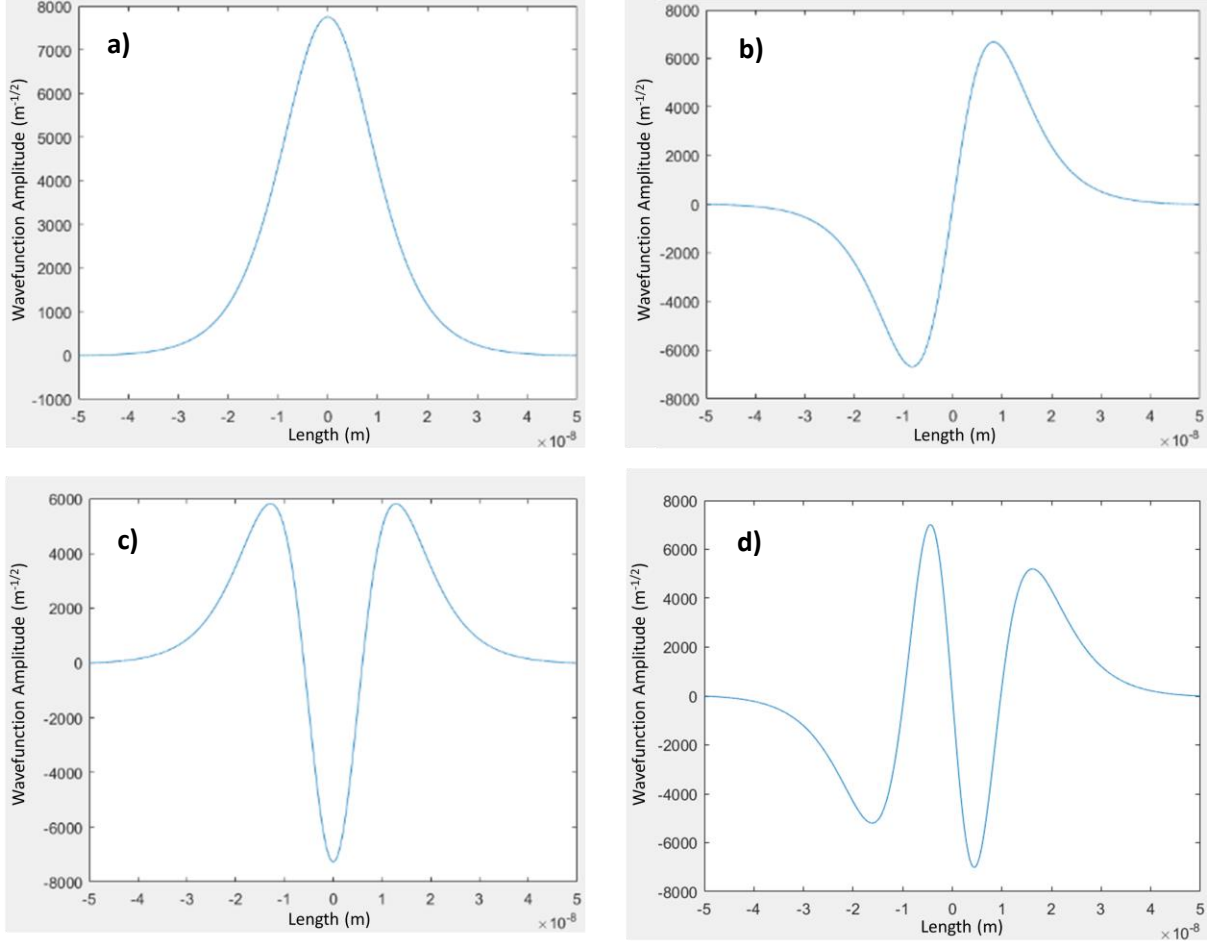
Figure 3. The first four wavefunctions for the soliton mass profile free particle. a, b, c, and d are, respectively, the $n = 1$, 2, 3, and 4 wavefunctions.

Variable Mass Quantum Harmonic Oscillator

Another interesting variable mass problem is the variable mass analogue to the quantum harmonic oscillator[12]. The eigenwaves for the variable mass quantum harmonic oscillator are similar to those for the traditional harmonic oscillator, and the energies are evenly spaced. For the following mass profile and potential[12]:

$$m(x) = \frac{m}{1+ax^2}, \quad \sigma = \frac{2m}{\hbar^2 a^2}, \tag{7}$$

$$V(x) = \frac{k^2}{\sigma}[\ln(1 + ax)]^2, \tag{8}$$

the eigenvalues are[12]:

$$E_n = \frac{\hbar^2}{2m}[k(2n + 1)]. \tag{9}$$

5

Because the mass and the reduced Planck constant were arbitrarily set to equal 1, the resulting eigenvalues are unit less. For $k = 2$ and $a = 0.1$, the calculated unit less eigenvalues are shown in Table 3. As expected, the eigenenergies are evenly spaced.

Table 3. Calculated eigenvalues for the variable mass quantum harmonic oscillator.

Eigenvalue	RK4 (unit less)	Basis Set (unit less)
1	0.9375	1.001248
2	3.1875	3.00124
3	5.09375	5.001224
4	7.046875	7.001199
5	9.023438	9.001167
6	11.01172	11.00113

The wavefunctions solved with the basis set expansion method are displayed in Figure 4. The wavefunctions resemble the Hermite polynomials multiplied by a Gaussian, the functions that solve the position-independent mass quantum harmonic oscillator problem.
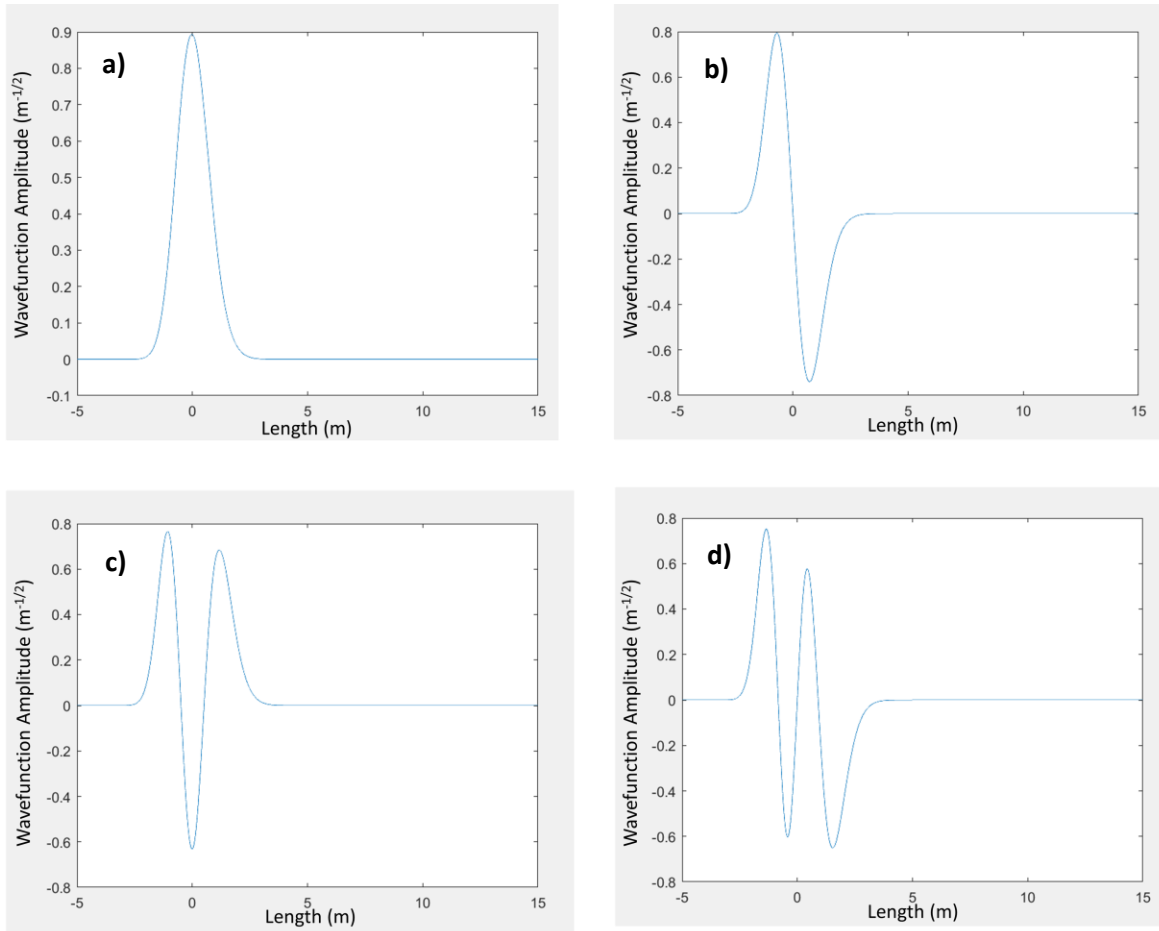
Figure 4. The first four wavefunctions for the variable mass quantum harmonic oscillator[12] solved via basis set expansion. **a**, **b**, **c**, and **d** are respectively the first, second, third, and fourth eigenfunctions.

Schrödinger Equation—Conclusion

Because several numerical methods independently give extremely similar values for the eigenenergy and because the numerical methods agree with analytical expressions, there is a high degree of confidence that the numerical methods developed adequately solve Schrödinger's equation.

For the Poisson-Schrödinger simulations, the basis set expansion method was used. It was found that the Runge-Kutta method could not be used with systems that had multiple quantum wells when the wells were too far apart from one another. When the wells are too far apart, they essentially behave as independent quantum wells. In such cases, numerical instabilities quickly manifest in the Runge-Kutta integration.

III. Fermi Level Determination

Once the eigenenergies and eigenfunctions have been calculated using the Schrödinger Equation, the total electron and hole spatial densities $n(x)$ and $p(x)$ are calculated with:

$$n(x) = \sum_j N_{j,n} |\psi_{j,n}(x)|^2, \tag{10}$$

$$p(x) = \sum_k N_{k,p} |\psi_{k,p}(x)|^2, \tag{11}$$

where $\psi_{j,n}$ and $\psi_{k,p}$ are, respectively, the eigenfunctions for each electron and hole subband and $N_{j,n}$ and $N_{k,p}$ are, respectively, the number of carriers per electron and hole subband. Each subband is an eigenenergy level with energy E_j or E_k (electrons or holes). The variables j and k index the electron and hole subbands respectively. The number of carriers in each subband is given by:

$$N_{j,n} = \int_{E_j}^{\infty} g_{2D,n}(E,x) f_{FD}(E) \, dE, \tag{12}$$

$$N_{k,p} = \int_{-\infty}^{E_k} g_{2D,p}(E,x) \big(1 - f_{FD}(E)\big) \, dE. \tag{13}$$

f_{FD} is the Fermi-Dirac distribution, which give the occupancy of states:

$$f_{FD}(E) = \frac{1}{1 + \exp(\frac{E - E_f}{kT})}. \tag{14}$$

$g_{2D,n}$ and $g_{2D,p}$ are the density of states for a 2D infinite well. The density of states essentially determines the number of states per energy level:

$$g_{2D,n} = \frac{m_n^*}{\pi \hbar^2}, \tag{15}$$

$$g_{2D,p} = \frac{m_p^*}{\pi \hbar^2}, \tag{16}$$

Evaluating Equations 12 and 13 gives:

$$N_{j,n} = \frac{kT m_n^*}{\pi \hbar^2} \ln[1 + \exp(\frac{E_f - E_j}{kT})], \tag{17}$$

$$N_{k,p} = \frac{kTm_p^*}{\pi\hbar^2} \ln[1 + \exp(\frac{E_p - E_f}{kT})\,]. \tag{18}$$

There are several physical conditions that can be used to determine the Fermi level. In a High Mobility Electron Transistor (HEMT), for example, the Fermi level is set by the Schottky barrier contact. For other devices, total charge neutrality determines the Fermi level. That is, the total number of negative charges equals the total number of positive charges:

$$n(x) + N(x) = p(x) + P(x). \tag{19}$$

In Equation 19, $n(x)$ and $p(x)$ represent thermally excited free electrons and holes, respectively. The thermally excited electrons reside in the conduction band and the thermally excited holes reside in the valence band. $N(x)$ and $P(x)$ represent negative and positive charges other than thermally excited electrons and holes. $N(x)$ and $P(x)$ could, for example, represent ionized acceptor and donor ions or defects. For the charge neutrality condition, the Fermi level can be determined by solving Equation 19 using the bisection method.

IV. Poisson Equation

Compared to the Schrödinger equation, the Poisson equation is much more straightforward:

$$-\frac{d}{dx}\left(\epsilon(x)\frac{d\phi}{dx}\right) = \rho(x). \tag{20}$$

$\epsilon(x)$ is the permittivity throughout the structure and $\rho(x)$ is the charge density:

$$\rho(x) = P(x) + p(x) - n(x) - N(x). \tag{21}$$

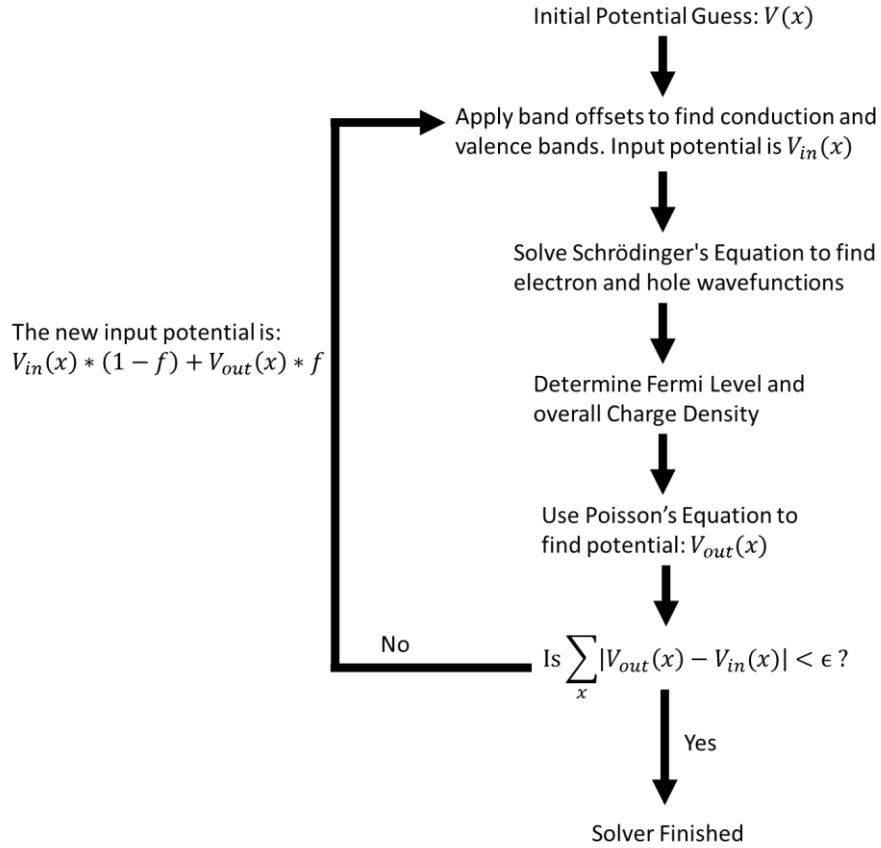Solving Equation 20 for the electrostatic potential yields:

$$\phi(x) = \int \left[\frac{1}{\epsilon(x)} \int -\rho(x)dx\right] dx \tag{22}$$

Equation 22 can be solved using finite differences. MATLAB has a built-in command called cumtrapz, which can performed numerical integration. The electric field may be discontinuous, but the displacement field is continuous throughout the structure. Unlike the Schrödinger equation, the numerical solutions to Equation 22 are trivial so no examples are shown. For an overall charge neutral structure, the electric field is zero at the beginning and at the endpoint of the structure.

V. Self-Consistent Iterations

The following self-consistent scheme was implemented:

Initial Potential Guess: $V(x)$

Apply band offsets to find conduction and valence bands. Input potential is $V_{in}(x)$

Solve Schrödinger's Equation to find electron and hole wavefunctions

Determine Fermi Level and overall Charge Density

Use Poisson's Equation to find potential: $V_{out}(x)$

Is $\sum_{x} |V_{out}(x) - V_{in}(x)| < \epsilon$?

No

The new input potential is:
$V_{in}(x) * (1 - f) + V_{out}(x) * f$

Yes

Solver Finished

Figure 5. Self-consistent iteration scheme used in the PS solver

Essentially, we start with an initial potential guess. After solving the coupled Poisson-Schrödinger equation, we get a potential function out. If this potential function is not the same as the input potential function for a given error limit, we create a new input potential function. This new input potential is an amalgamation of the original input and the corresponding output. The f factor in Figure 5 determines the mixing of the input and output potentials. If the f factor is too large, the solver diverges. But if the f factor is too small, it takes a long time for the solver to converge to a solution. This iterative process continues until we satisfy the equality of the input and output potential functions at some error limit. Depending on the discretization spacing and the number of orthogonal basis functions used to solve Schrödinger's equation (Appendix A), the total program runtime could vary from several minutes to several hours.

VI. HEMT Transistor Test Case

Having described the details of the PS solver, it is now used to simulate a GaAs/AlGaAs High Electron Mobility Transistor (HEMT). In an HEMT, the heterojunction between GaAs and AlGaAs forms a 2D electron gas (2DEG). A metal contact is attached to the GaAs side, forming a Schottky barrier. The HEMT properties are controlled by manipulating the 2DEG density with the gate voltage. HEMT transistors are commonly used in high frequency applications such as cell phones and radio transmitters. A detailed description of the simulation parameters is given in Appendix D. The resulting PS-solved band structure is given in Figure 6.
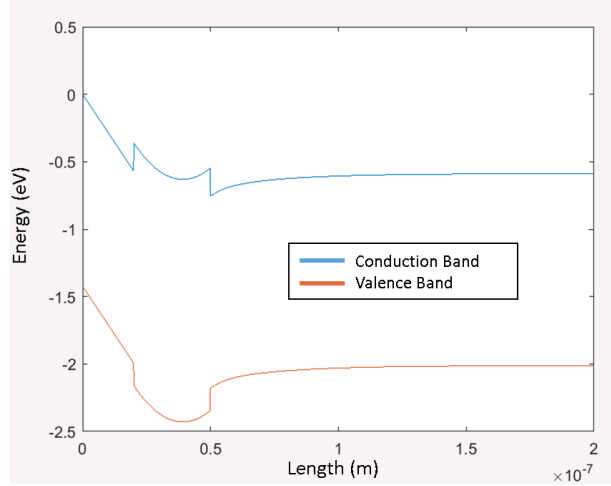
Figure 6. Simulated HEMT structure. See Appendix D for a detailed overview of the simulation parameters.

The results of the developed PS solver (Figure 6) agree with literature on HEMTs[13]. The same HEMT structure was also simulated with the 1D heterostructure tool on nanohub.com[14] (Figure 7). Any slight differences between Figure 6 and 7 can likely be attributed to the different constant values used.
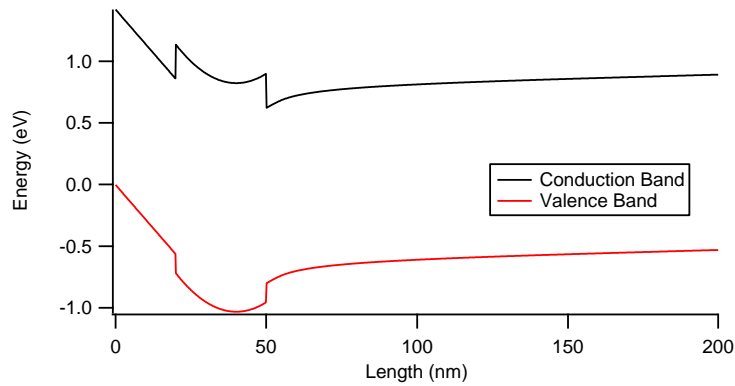

Figure 7. The same HEMT in Figure 6 simulated using the 1D heterostructure tool on nanohub.com[14].

VII. Using Poisson-Schrödinger to Simulate the LaAlO$_3$/SrTiO$_3$ Interface

The interface between two insulating oxides, LaAlO$_3$ (LAO) and SrTiO$_3$ (STO), has been found to have many interesting properties, including the formation of a 2DEG, superconductivity, and ferromagnetism[15,16]. Previous studies have simulated the electronic reconstruction occurring at the LAO/STO interface using a Poisson-Schrödinger solver [1,16-19]. Here, some of the results of Z. Gu et al.[1] are replicated to show that the PS solver can be adapted for a wide-bandgap complex oxide system.

The band structure for a 10 unit cell LAO/100 nm STO substrate at 300 Kelvin is shown in Figure 8. A zoomed in view of the conduction band (Figure 9) shows that the band bending is around 0.26 eV, as previously reported by Z. Gu[1]. The calculated electron sheet density was $1.66*10^{14}$ cm^{-2}, in agreement with literature[1].
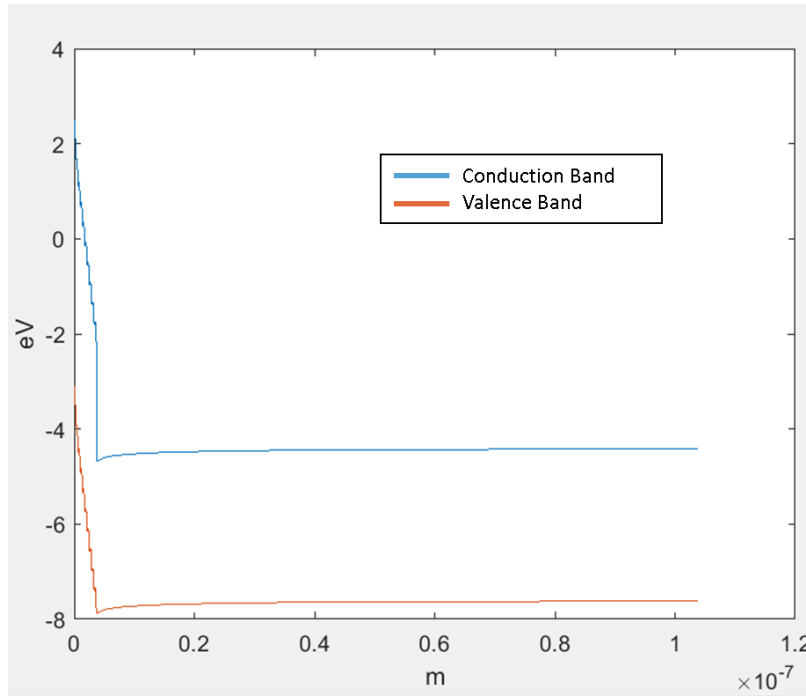
Figure 8. Self-consistent PS results for a 10 unit cell LAO/100 nm STO structure.
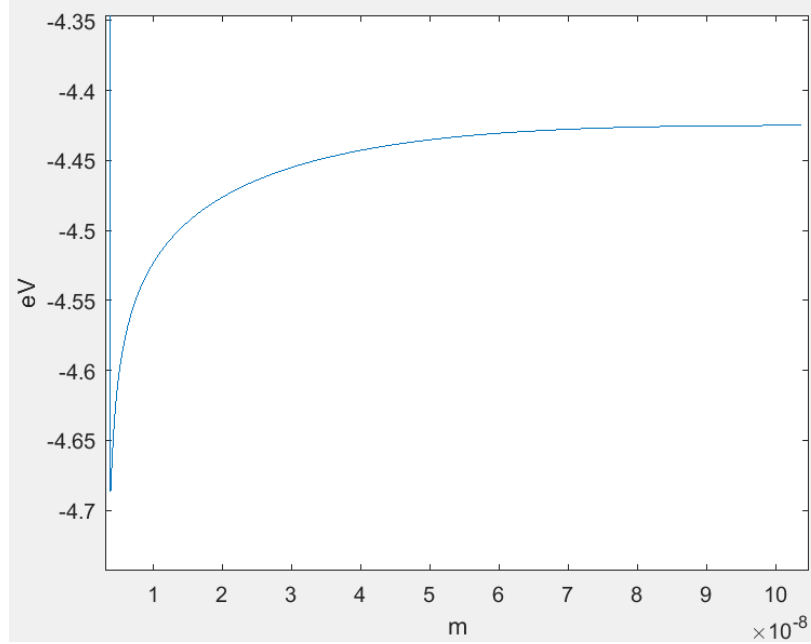
Figure 9. Zoomed in view of the conduction band in Figure 8. The calculated band bending agrees with literature[1].
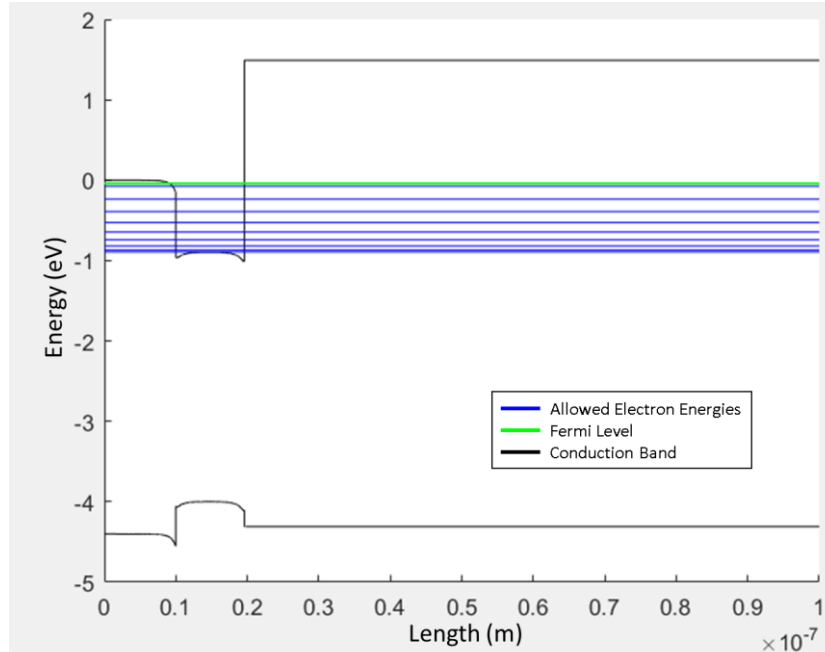
VIII. Conclusion

A self-consistent Poisson Schrödinger solver was developed using MATLAB. Although numerous PS solvers exist, a home-built PS solver provides a tremendous learning experience and offers greater control over simulation parameters. The step-by-step discussion of the solver shows that all the components of the PS solver works as intended. Future work with the PS solver will include the simulation of complex oxide heterostructure grown by pulsed laser deposition. The goal is to correlate the PS-simulated band structures with experimental photoluminescence done on the heterostructures. Perhaps, the PS-solver can even be used in materials design; it can be used to propose interesting material structures to grow. Ultimately, the PS solver provides a unique opportunity to link theory and experiment.

IX. Future Work on Complex Oxide Heterostructures

The ultimate goal is to simulate complex oxide heterostructures and correlate experimental photoluminescence experiments with theoretical simulations. The materials of interest are heterostructures of $CaSnO_3$ (CSO) and Lanthanum-doped $BaSnO_3$ ($Ba_xLa_{1-x}SnO_3$, BLSO) grown in the [001] direction by pulsed laser deposition on a $(LaAlO_3)_{0.3}(Sr_2TaAlO_6)_{0.7}$ (LSAT) substrate. The band alignments[20, 21] for CSO/BLSO/LSAT structure are shown in Figure 8.

Figure 8. Band alignment in a CSO/BLSO/LSAT heterostructure.

The band offsets indicate that electron confinement can occur in the BLSO layer. But, for a 2DEG to form, a source of electrons must be present. At the interface between a polar and a non-polar material, such as in the much-studied $LaAlO_3$/$SrTiO_3$ interface, the polar catastrophe can induce a 2DEG to form in the non-polar material[21]. $CaSnO_3$ grown in the [001] direction, however, is non-polar.

One possible explanation for the 2DEG electron source is that the Lanthanum dopants function as n-type donors in the BLSO[22-26]. If this is the case, it can be assumed that the La dopant atoms ionize, giving off one free electron, and leaving a positive ion. For a 5% La-doped BSO sample, complete ionization of the La atoms gives a positive ion density of $7.18*10^{20}$ cm^{-3}. Since each ionized La atom corresponds to a free electron, the electron density is $7.18*10^{20}$ cm^{-3}; this agrees with reported Hall measurements on thin film and ceramic BLSO[22-26]. Interestingly, un-doped BSO ($BaSnO_3$) is insulating and has a negligible electron density[24].

Continuing with the n-type doped BLSO idea, Equation 19 can be used to find the Fermi level. In Equation 19, $P(x)$ is the density of the ionized La dopants and $n(x)$ is the electron density, or the 2DEG density. $N(x)$ is assumed to be zero (there are no negatively charged impurities/dopants), and $p(x) \approx 0$ because the Fermi level will be far above the valence band and very few holes will be thermally created. With these parameters, the 2DEG electron sheet density of a CSO/BLSO structure of 10/9.6 nm was found to be $6.89*10^{14}$ cm^{-2}, which agrees with reports of the 2DEG electron density in $LaInO_3$ /BLSO heterostructures[26]. Figure 9 shows a preliminary PS-solved band structure for a CSO/BLSO structure of 10/9.6 nm.

Figure 9. Self-consistent Poisson-Schrödinger results on a CSO/BLSO structure of 10/9.6 nm on a LSAT substrate.

As the dopant level decreases, it is proposed that the 2DEG electron sheet density decreases because ionized Lanthanum atoms are responsible for giving electrons. As the 2DEG electron sheet density decreases the band bending, the bending near the heterojunction interfaces, decreases. In a CSO/BSO heterojunction, a quantum well forms, but no electrons occupy the quantum well. As such, the CSO/BSO heterojunction experiences no band bending—the quantum well is a finite well such as that shown in Figure 1.

Much work remains in understanding the CSO/BLSO interface and in understanding complex oxide interfaces in general. Nevertheless, the major point of this report is that the developed PS-solver works.

X. References

[1] Z. Gu et al., "Giant enhancement in the ferroelectric field effect using a polarization gradient," Applied Physics Letters **107**, 162901, Oct. 2015. doi: http://dx.doi.org/10.1063/1.4933095

[2] A. Janotti et al., "Controlling the density of the two-dimensional electron gas at the $SrTiO_3$/$LaAlO_3$ interface," Phys. Rev. B **86**, 241108(R), Dec. 26, 2012. doi: http://dx.doi.org/10.1103/PhysRevB.86.241108

[3] M. J. Hargrove, A. K. Henning, J. A. Slinkman and J. C. Bean, "Quantum mechanical modeling of the charge distribution Si/Si/sub 1-x/Ge/sub x/Si p-channel MOSFET," Electron Devices Meeting, 1994. IEDM '94. Technical Digest., International, San Francisco, CA, USA, 1994, pp. 735-738. doi: 10.1109/IEDM.1994.383284

[4] Ram-Mohan LR, Yoo KH, Moussa J. The Schrödinger-Poisson self-consistency in layered quantum semiconductor structures Journal of Applied Physics. 95: 3081-3092. DOI: 10.1063/1.1649458

[5] 1D Poisson. G Snider - URL, http//www. nd. edu/~ gsnider, 2007

[6] S. Birner et al., "nextnano: General Purpose 3-D Simulations," in IEEE Transactions on Electron Devices, vol. 54, no. 9, pp. 2137-2142, Sept. 2007. doi: 10.1109/TED.2007.902871

[7] Godfrey S. Beddard, "Solution of the Schrödinger Equation for One-Dimensional Anharmonic Potentials: An Undergraduate Computational Experiment," Journal of Chemical Education 2011 88 (7), 929-931. DOI: 10.1021/ed1000137

[8] John M Blatt, Practical points concerning the solution of the Schrödinger equation, Journal of Computational Physics, Volume 1, Issue 3, 1967, Pages 382-396, ISSN 0021-9991, http://dx.doi.org/10.1016/0021-9991(67)90046-0.

[9] Vern Lindberg, "Finite Square Well," RIT. https://people.rit.edu/vwlsps/314_w07/FiniteSquareWell.pdf

[10] J. P Killingbeck et al., "The Schrödinger equation with position-dependent mass," Journal of Physics A: Mathematical and Theoretical, Volume 44, Number 28, June 2011. doi: 10.1088/1751-8113/44/28/2852080

[11] M. S. Cunha and H. R. Christiansen, "Analytic results in the position-dependent mass Schrodinger problem," Communications in Theoretical Physics, vol. 60, no. 6, pp. 642-650, December 2013. http://iopscience.iop.org/0253-6102/60/6/02

[12] M. Tchoffo et al. "Quantum harmonic oscillator with position-dependent mass in the displacement operator formalism," Physica Scripta, vol. 89, no. 10, Aug. 2014. http://iopscience.iop.org/1402-4896/89/10/105201

[13] Tan, I-H. and Snider, G. L. and Chang, L. D. and Hu, E. L., "A self-consistent solution of Schrödinger–Poisson equations using a nonuniform mesh," Journal of Applied Physics, 68, 4071-4076 (1990), DOI:http://dx.doi.org/10.1063/1.346245

[14] 1D Heterostructure Tool. https://nanohub.org/tools/1dhetero/

[15] A. Ohtomo et al., "A high-mobility electron gas at the LaAlO3/SrTiO3 heterointerface," Nature 427, 423-426 (2004).

[16] M. A. Islam et al., "Surface Chemically Switchable Ultraviolet Luminescence from Interfacial Two-Dimensional Electron Gas," Nano Lett. 16, 681-687 (2016). doi: 10.1021/acs.nanolett.5b04461

[17] A. Janotti et al., "Controlling the density of the two-dimensional electron gas at the $SrTiO_3$/$LaAlO_3$ interface," Physical Review B **86**, 241108 (2012). doi: http://dx.doi.org/10.1103/PhysRevB.86.241108

[18] S. Su et al. "Electron transport of LaAlO3 and SrTiO3 band insulators," Journal of Applied Physics 113, 093709 (2013). doi: 10.1063/1.4794507

[19] S. Gariglio et al. "Electron confinement at the $LaAlO_3$/$SrTiO_3$ interface," Journal of Physics: Condensed Matter 27 283201 (2015). doi: http://iopscience.iop.org/0953-8984/27/28/283201

[20] Ryan B. Comesa, Peng Xub, Bharat Jalanb and Scott A. Chambersa, "Band alignment of epitaxial SrTiO3 thin films with (LaAlO3)0.3-(Sr2AlTaO6)0.7 (001)", Applied Physics Letters **107**, 131601 (2015) http://dx.doi.org/10.1063/1.4932063

[21] L Bjaalie, B Himmetoglu, L Weston, A Janotti and C G Van de Walle, "Oxide interfaces for novel electronic applications" New J. Phys. 16 (2014) 025005. http://iopscience.iop.org/1367-2630/16/2/025005

[22] H. F. Wang et al., "Transparent and conductive oxide films with the perovskite structure: La- and Sb-doped $BaSnO_3$," Journal of Applied Physics **101**, 106105 (2007). doi: 10.1063/1.2736629

[23] H. J. Kim et al., "Physical properties of transparent perovskite oxides $(Ba,La)SnO_3$ with high electrical mobility at room temperature," Physical Review B **86**, 165205 (2012). doi: 10.1103/PhysRevB.86.165205

[24] S. Upadhyay et al., "Synthesis, structure, and electrical behavior of lanthanum-doped barium stannate," Journal of Physics D: Applied Physics 37 1483 (2004). http://iopscience.iop.org/0022-3727/37/10/011

[25] D. Seo et al., "Infrared-optical spectroscopy of transparent conducting perovskite $(La,Bn)SnO_3$ thin films," Applied Physics Letters **104**, 022102 (2014). doi: 10.1063/1.48617761

[26] U. Kim et al., "Conducting interface states at $LaInO_3/BaSnO_3$ polar interface controlled by Fermi level," APL Mater. **4** 071102 (2016). doi: 10.1063/1.4959960

[27] GaAs. http://www.ioffe.ru/SVA/NSM/Semicond/GaAs/bandstr.html

[28] $Al_xGa_{1-x}As$. http://www.ioffe.ru/SVA/NSM/Semicond/AlGaAs/bandstr.html

[29] J. Batey and S. L. Wright, "Energy band alignment in GaAs: (Al, Ga)As heterostructures: The dependence on alloy composition, J. Appl. Phys. **59**, 200 (1986). doi: http://dx.doi.org/10.1063/1.336864

[30] J. R. Waldrop, "Direct variation of metal-GaAs Schottky barrier height by the influence of interface S, Se, and Te," Appl. Phys. Lett **47**, 1301 (1985). doi: http://dx.doi.org/10.1063/1.96312

Appendix A—Basis Set Expansion

The following discussion is modeled after[7].

Let $\{f_i(x)\}$ be a set of orthogonal functions such that:

$$\int f_m{}^* f_n dx = \delta_{m,n} = \begin{cases} 0, m \neq n \\ 1, m = n \end{cases} \tag{A1}$$

Included in $\{f_i(x)\}$ are the functions $f_1, f_2, \dots, f_N$. There are N total functions in the set. The eigenfunctions for an infinite square well (sine waves of varying frequency) were used for the simulations:

$$f_i(x) = \sqrt{\frac{2}{a}} \sin\left(\frac{i\pi}{a}x\right), i = 1,2,3 \dots N, \tag{A2}$$

where a is the length of the infinite box, which is equal to the length of the potential function simulated.

The Schrödinger Equation is

$$\hat{H}\psi_i(x) = E_i\psi_i(x), \tag{A3}$$

where the Hamiltonian operator is:

$$\hat{H} = \frac{-\hbar^2}{2}\frac{d}{dx}\left(\frac{1}{m(x)}\frac{d}{dx}\right) + V(x). \tag{A4}$$

Let ψ_i be a linear combination of the orthogonal functions. A set of functions $\{\psi_i\}$ will satisfy Schrödinger's equation and i is used to index through this set. Each ψ_i will have a different set of coefficients $\{c_n\}$, where the coefficients are used to construct the linear combination:

$$\psi_i(x) = c_{1,i}f_1 + c_{2,i}f_2 + c_{3,i}f_3 + \cdots c_{N,i}f_N = \sum_n c_{n,i}f_n(x). \tag{A5}$$

For each ψ_i there is also a corresponding eigenenergy E_i.

Multiplying both sides of Equation A3 by f_k,

$$f_k\hat{H}\psi_i(x) = f_k E_i\psi_i(x), \tag{A6}$$

and integrating

$$\int f_k\hat{H}\psi_i(x)\,dx = \int f_k E_i\psi_i(x)\,dx = E_i\int f_k\psi_i(x)\,dx \tag{A7}$$

In Equation A7, the term E_i is a constant.

Remember ψ_i is a linear combination, so the rightmost side of Equation A7 simplifies to:

$$E_i\int f_k\psi_i(x)\,dx = E_i\int f_k \sum_n c_{n,i}f_n(x)\,dx = E_i\int \sum_n c_{n,i} * f_k f_n(x)\,dx = E_i c_{k,i} \tag{A8}$$

The above evaluates to $E_i c_{k,i}$ because of the orthogonality of the functions $\{f_i(x)\}$. For all values other than $i = k$, the integral is zero.

The left hand side of Equation A7 can also be expanded:

$$\int f_k\hat{H}\psi_i(x)\,dx = \int f_k\hat{H}\sum_n c_{n,i}f_n(x)\,dx = \int \sum_n c_{n,i} * f_k\hat{H}f_n(x)\,dx = \sum_n c_{n,i}\int f_k\hat{H}f_n(x)dx. \tag{A9}$$

Denoting

$$\int f_k \hat{H} f_n(x)dx = H_{k,n} \tag{A10}$$

Then combing Equations A7 through A10 yields:

$$\sum_n c_{n,i} H_{k,n} = E_i c_{k,i}. \tag{A11}$$

The index k of $H_{k,i}$ refers to the f_k function originally used to multiply the linear combination wavefunction. f_k belongs to the set of orthogonal functions $\{f_i(x)\}$, so $k = 1,2,\dots,N$ where N is the total number of elements in $\{f_i(x)\}$. Because the f_k chosen in Equation A6 is arbitrary, we can apply an additional summation to Equation A11 over the index k to get:

$$\sum_k^N \sum_n c_{n,i} H_{k,n} = \sum_k^N E_i c_{k,i}. \tag{A12}$$

For a few terms,

$$c_{1,i} H_{1,1} + c_{2,i} H_{1,2} + c_{3,i} H_{1,3} + \dots + c_{N,i} H_{1,N} = E_i c_{1,i}$$

$$c_{1,i} H_{2,1} + c_{2,i} H_{2,2} + c_{3,i} H_{2,3} + \dots + c_{N,i} H_{2,N} = E_i c_{2,i} \tag{A13}$$

$$c_{1,i} H_{3,1} + c_{2,i} H_{3,2} + c_{3,i} H_{3,3} + \dots + c_{N,i} H_{3,N} = E_i c_{3,i}.$$

If we let $\vec{c}_i = [c_{1,i}, c_{2,i}, c_{3,i}, \dots, c_{N,i}]$

and $\boldsymbol{H} = \begin{bmatrix} H_{1,1} & H_{1,2} & H_{1,3} & \cdots & H_{1,N} \\ H_{2,1} & H_{2,2} & H_{2,3} & \cdots & H_{2,N} \\ H_{3,1} & H_{3,2} & H_{3,3} & \cdots & H_{3,N} \\ \vdots & \vdots & \vdots & \ddots & \vdots \\ H_{N,1} & H_{N,2} & H_{N,3} & \cdots & H_{N,N} \end{bmatrix}$.

The problem turns into an eigenvalue problem:

$$\boldsymbol{H}\vec{c}_i = E_i \vec{c}_i \tag{A14}$$

The resulting matrix will be of size NxN. $N = 200$ is more than sufficient, and MATLAB can easily solve the eigenvalue problem. The solutions to Equation A14 will be a set of $\{E_i\}$ and $\{\vec{c}_i\}$.

The resulting allowed wavefunctions can be found by:

$$\psi_i = \vec{c}_i \cdot \vec{f}, \tag{A15}$$

where $\vec{f} = [f_1, f_2, f_3, \dots f_N]$. The set of $\{E_i\}$ is the allowed eigenenergies.

The boundary conditions $\psi_i(x = 0) = 0$ and $\psi_i(x = x_{end}) = 0$ are naturally satisfied because the set of orthogonal functions used have $\psi_i(x = 0) = 0$ and $\psi_i(x = x_{end}) = 0$.

Appendix B—Numerov's Method

For the constant mass Schrödinger equation,

$$\frac{d^2\psi}{dx^2} = f(x)\psi(x), \tag{B1}$$

where

$$f(x) = \frac{2m}{\hbar^2}[V(x) - E], \tag{B2}$$

Numerov's method gives[8]:

$$[1 - T(x+h)]\psi(x+h) + [1 - T(x-h)]u(x-h) \approx [2 + 10T(x)]u(x), \tag{B3}$$

where $T(x) = \frac{h^2}{12}f(x)$ and h is the discretization spacing. The error associated with Numerov's method is sixth order $O(h^6)$.

The integration can be performed from the left to the right and from the right to the left. Left to right integration means we start at $x = x_{init}$ and incrementally integrate to $x = x_{end}$; these wavefunctions will be termed $\psi_{L \to R}$. For right to left integration, we start at $x = x_{end}$ and detrimentally integrate to $x = x_{init}$; these wavefunctions will be termed $\psi_{R \to L}$.

$\psi_{L \to R}(x)$ is found by iteratively solving Equation B3 for $\psi(x+h)$. The initial conditions are: $\psi_{L \to R}(x_{init}) = 0$ and $\psi_{L \to R}(x_{init} + h) = \epsilon$, where ϵ is an arbitrarily small number (10^{-100}).

$\psi_{R \to L}(x)$ is found by iteratively solving Equation B3 for $\psi(x-h)$. The initial conditions are: $\psi_{R \to L}(x_{end}) = 0$ and $\psi_{R \to L}(x_{end} - h) = \epsilon$, where ϵ is an arbitrarily small number (10^{-100}).

The integrated wavefunction $\psi_{L \to R}$ is a wavefunction if $\psi_{L \to R}(x_{end}) = 0$, and the integrated wavefunction $\psi_{R \to L}$ is a wavefunction if $\psi_{R \to L}(x_{init}) = 0$. In the shooting method we search for eigenenergies E that satisfy these boundary conditions. The shooting method, however, is prone to numerical instabilities and oftentimes, the boundary conditions cannot be met exactly.

Therefore the crossfire method was implemented[3]. In the crossfire method, we integrate from x_{init} to x_{patch}, a patching point, using $\psi_{L \to R}$. We then integrate from x_{end} to x_{patch} using $\psi_{R \to L}$. Essentially we numerically integrate in two different directions and patch the two results at a certain point. An energy E is an eigenenergy if:

$$\psi_{R \to L}\left(x = x_{patch}\right) * \frac{d}{dx}\psi_{L \to R}\left(x = x_{patch}\right) - \psi_{L \to R}\left(x = x_{patch}\right) * \frac{d}{dx}\psi_{R \to L}\left(x = x_{patch}\right) = 0. \tag{B4}$$

The condition specified in Equation B4 dictates that the patching between $\psi_{L \to R}$ and $\psi_{R \to L}$ creates a continuous function. The eigenenergies E that lead to wavefunctions $\psi_{L \to R}$ and $\psi_{R \to L}$ satisfying Equation C4 are found by minimizing the left hand side of Equation B4 using the bisection method.

That is, the left hand side of Equation B4 is a function that depends on the energy E: the wavefunctions depend on E via Equations B3. Therefore the goal is to find the E that minimize $f(E)$, where

$$f(E) = \psi_{R \to L}\left(x = x_{patch}\right) * \frac{d}{dx}\psi_{L \to R}\left(x = x_{patch}\right) - \psi_{L \to R}\left(x = x_{patch}\right) * \frac{d}{dx}\psi_{R \to L}\left(x = x_{patch}\right). \tag{B5}$$

For the finite square well example in Figure 1, $f(E)$ (Equation B5) is plotted in Figures B1 and B2. The zero crossings of $f(E)$ are the eigenenergies and match up with the values in Table 1.
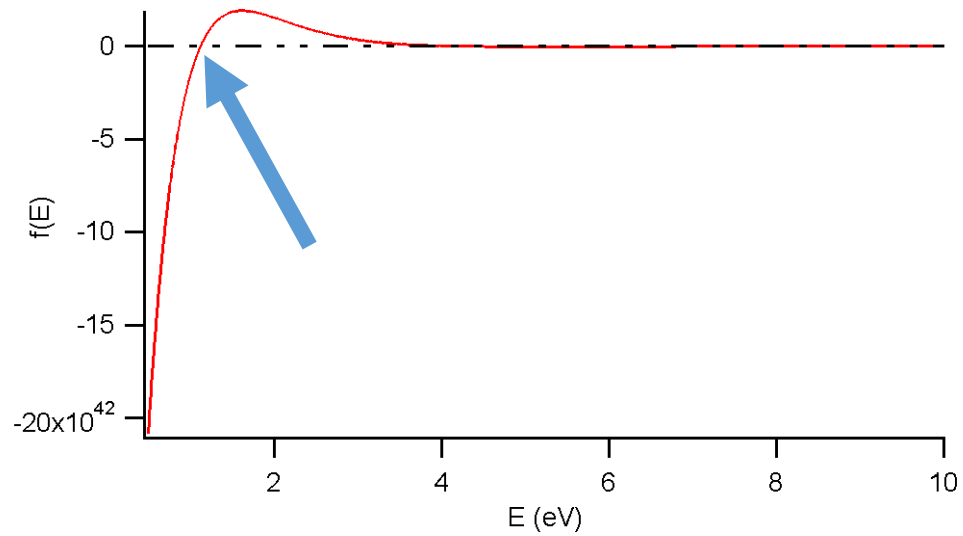
Figure B1. $f(E)$ (Equation B5) for the finite square well of Figure 1. The zero crossings are eigenvalues.
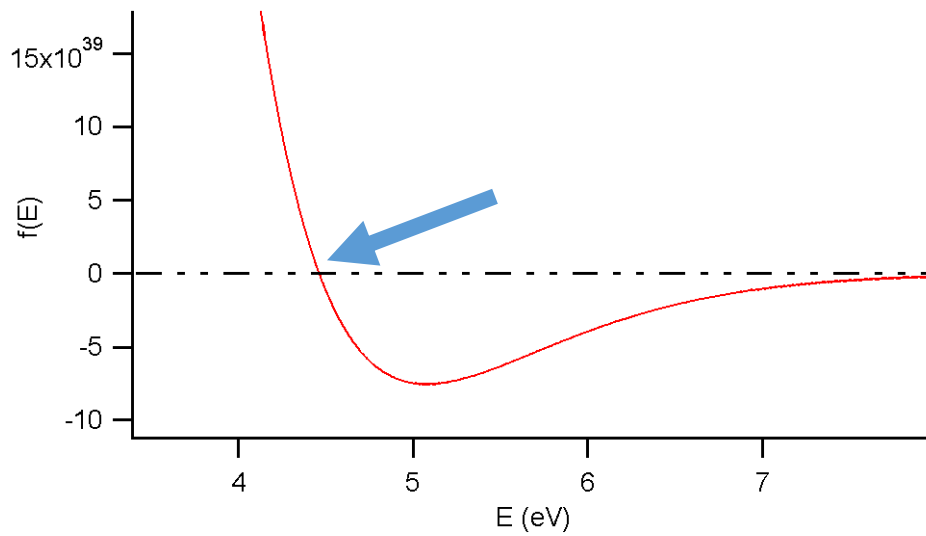
Figure B1. $f(E)$ (Equation B5) for the finite square well of Figure 1. Zoomed in to show the second zero crossing.

Appendix C—Runge-Kutta Method

First the variable mass Schrödinger equation can be rewritten as a system of two first order differential equations. We start with,

$$\left[\frac{-\hbar^2}{2}\frac{d}{dx}\left(\frac{1}{m(x)}\frac{d}{dx}\right) + V(x)\right]\psi(x) = E\psi(x) \tag{C1}$$

After several manipulations,

$$\frac{d^2}{dx^2}\psi(x) = -\frac{2m(x)}{\hbar^2}\big(E - V(x)\big)\psi(x) + \frac{\frac{d}{dx}m(x)}{m(x)}\frac{d}{dx}\psi(x) = \alpha(x)A(x) + \beta(x)B(x) \tag{C2}$$

$$A(x) = \psi(x) \tag{C3}$$

$$B(x) = \frac{d}{dx}\psi(x) = \frac{d}{dx}A(x) \tag{C4}$$

$$\alpha(x) = -\frac{2m(x)}{\hbar^2}\big(E - V(x)\big) \tag{C5}$$

$$\beta(x) = \frac{\frac{d}{dx}m(x)}{m(x)} \tag{C6}$$

Ultimately, we arrive at:

$$\frac{d}{dx}B(x) = \alpha(x)A(x) + \beta(x)B(x) = g(A, B, x) \tag{C7}$$

$$\frac{d}{dx}A(x) = B(x) = f(A, B, x) \tag{C8}$$

The fourth order Runge-Kutta algorithm can be used to numerically solve for both A and B:

$$k_1 = h * f(A, B, x_n) = h * B(x_n) \tag{C9}$$

$$l_1 = h * g(A, B, x_n) = h * [\alpha(x_n)A(x_n) + \beta(x_n)B(x_n)] \tag{C10}$$

$$k_2 = h * f\left(A + \frac{k_1}{2}, B + \frac{l_1}{2}, x_{n+1/2}\right) = h * [B(x_n) + \frac{l_1}{2}] \tag{C11}$$

$$l_2 = h * g\left(A + \frac{k_1}{2}, B + \frac{l_1}{2}, x_{n+1/2}\right) = h * \left[\alpha(x_{n+1/2})\left[A(x_n) + \frac{k_1}{2}\right] + \beta(x_{n+1/2})\left[B(x_n) + \frac{l_1}{2}\right]\right] \tag{C12}$$

$$k_3 = h * f\left(A + \frac{k_2}{2}, B + \frac{l_2}{2}, x_n\right) = h * [B(x_n) + \frac{l_2}{2}] \tag{C13}$$

$$l_3 = h * g\left(A + \frac{k_2}{2}, B + \frac{l_2}{2}, x_{n+1/2}\right) = h * \left[\alpha(x_{n+1/2})\left[A(x_n) + \frac{k_2}{2}\right] + \beta(x_{n+1/2})\left[B(x_n) + \frac{l_2}{2}\right]\right] \tag{C14}$$

$$k_4 = h * f(A + k_3, B + l_3, x_{n+1}) = h * [B(x_{n+1}) + l_3] \tag{C15}$$

$$l_4 = h * g(A + k_3, B + l_3, x_{n+1}) = h * \left[\alpha(x_{n+1})[A(x_n) + k_3] + \beta(x_{n+1})[B(x_n) + l_3]\right] \tag{C16}$$

$$A(x_{n+1}) = A(x_n) + \frac{1}{6}(k_1 + 2k_1 + 2k_2 + k_4) \tag{C17}$$

$$B(x_{n+1}) = B(x_n) + \frac{1}{6}(l_1 + 2l_1 + 2l_2 + l_4) \tag{C18}$$

Evaluating Equations C9 through C18 allows for integration from the left hand to the right hand side. To backwards integrate, from the right hand side to the left hand side, the potential function and the mass function are inverted and the left to right integration formulae are used. After A and B are found they are simply inverted.

The two boundary conditions supplied for the left to right integration were:

$$A(x = x_{init}) = 0 \tag{C19}$$

$$B(x = x_{init}) = 0 \tag{C20}$$

The two boundary conditions supplied for the right to left integration were:

$$A(x = x_{end}) = 0 \tag{C21}$$

$$B(x = x_{end}) = 0 \tag{C22}$$

Because $B(x) = \frac{d}{dx}\psi(x)$, the Runge-Kutta method will not satisfactorily solve for potentials where the wavefunction abruptly goes to zero and $\frac{d}{dx}\psi(x) \neq 0$.

The crossfire method[3], discussed in Appendix B, was used to find the eigenvalues and eigenfunctions.

Appendix D—HEMT Simulation

A GaAs/AlGaAs HEMT was simulated. The following constants were used[27-30]:

GaAs

- $0.063m_e$ effective mass (m_e = electron mass)
- 1.424 eV band gap
- 12.9 static dielectric constant

$Al_xGa_{1-x}As$ (x = 0.3)
- $0.0879m_e$ effective mass
- 1.7981 eV band gap
- 12.048 static dielectric constant
- Valence Band Offset = 0.55 * x (AlGaAs valence band is below GaAs valence band)

Schottky Barrier = 0.69 eV below the E_c(x = 0) point

The heterostructure consisted of GaAs/AlGaAs/GaAs in a 20/30/150 nm thick arrangement. The conduction and valence band of the HEMT without any PS solving is given in Figure D1.
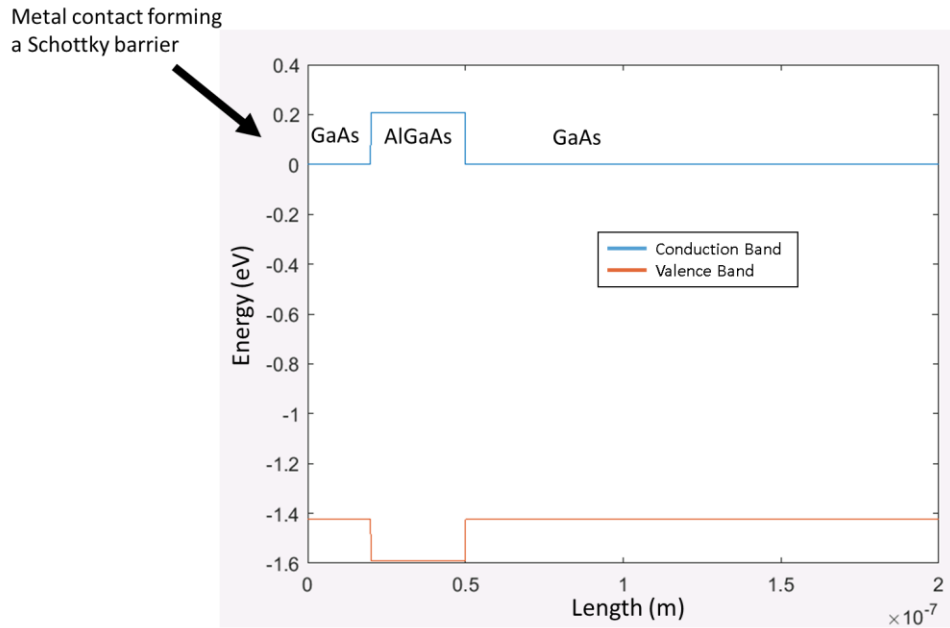

Figure D1. Band structure for the HEMT prior to any PS solving.

Both GaAs layers were doped with 10^{14} cm^{-3} positive ions and the AlGaAs layer was doped with 10^{18} cm^{-3} positive ions. Two physical boundary conditions are necessary for the HEMT. First, the Fermi level for a HEMT is not determined by total charge neutrality, but rather by a Schottky barrier. Second, the electric field at the rightmost end of the HEMT is zero; E_c(x = 200 nm) = 0 V/m. Figure D2 shows the energy levels (blue) and Fermi level (green) in the HEMT. Figure D3 shows the electric field in the HEMT.
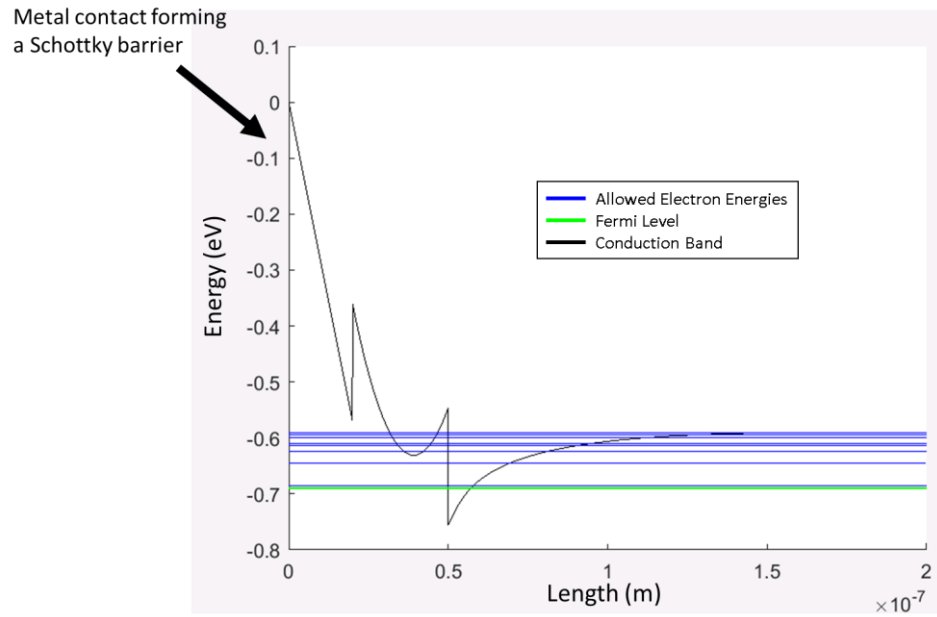
Figure D2. The electron eigenenergies and the Fermi level for the HEMT structure.
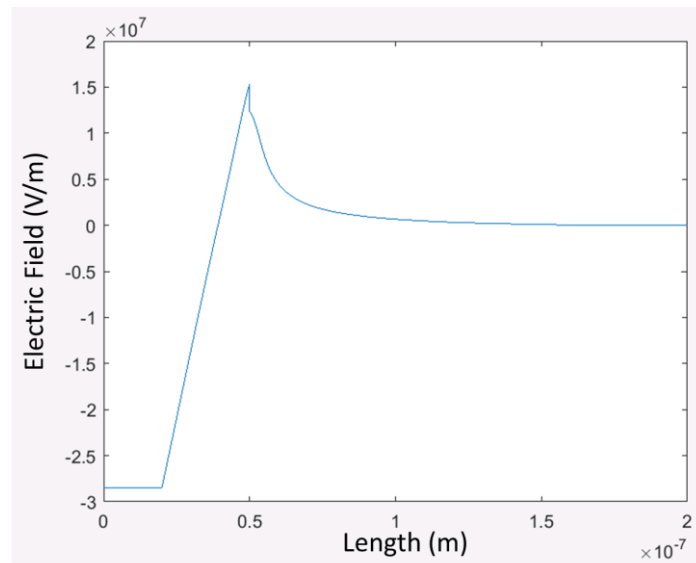
Figure D3. The electric field in the HEMT structure.